

Sub-femtosecond Electron Transport in a Nanoscale Gap

Markus Ludwig¹, Garikoitz Aguirregabiria², Felix Ritzkowski¹, Tobias Rybka¹, Dana Codruta Marinica³, Javier Aizpurua², Andrei G. Borisov³, Alfred Leitenstorfer¹, Daniele Brida^{1,4,*}

¹ Department of Physics and Center for Applied Photonics, University of Konstanz, D-78457 Konstanz, Germany

² Centro de Física de Materiales, Centro Mixto CSIC-UPV/EHU and Donostia International Physics Center (DIPC), 20018 Donostia-San Sebastián, Spain

³ Institut des Sciences Moléculaires d'Orsay - UMR 8214, CNRS-Université Paris Sud, Bâtiment 520, Orsay Cedex 91405, France.

⁴ Physics and Materials Science Research Unit, University of Luxembourg, 162a avenue de la Faïencerie, L-1511 Luxembourg, Luxembourg

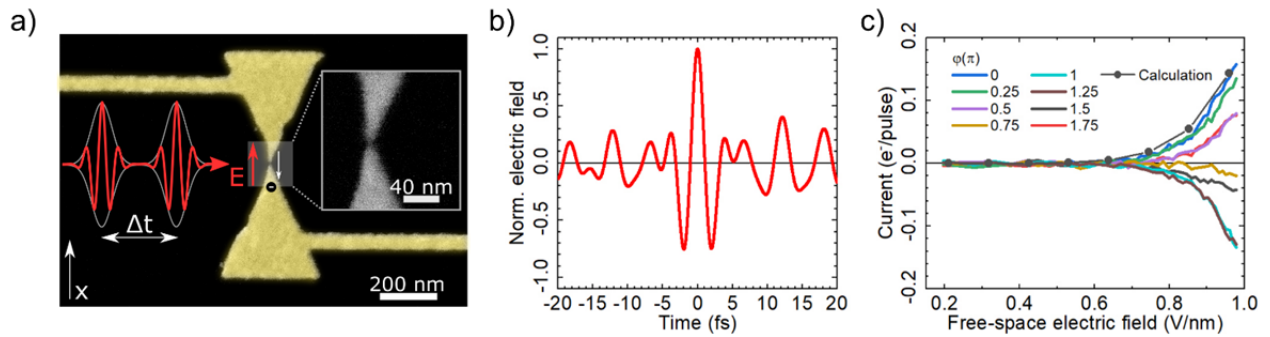
* e-mail: daniele.brida@uni.lu

We employ near-infrared single-cycle pulse pairs to drive interferometric autocorrelations of the ultrafast current produced by optical field emission at the nanogap of a single plasmonic nanocircuit. This highly nonlinear process depends fully on the precise temporal field profile of the optical driving pulse. Current autocorrelations are acquired with sub-femtosecond temporal resolution as a function of both pulse delay and absolute carrier-envelope phase. In this way, we study the ultrafast dynamics of electronic nanotransport. Quantitative modelling of the experiments enables us to monitor the spatio-temporal evolution of the electron density and currents induced in the system and to elucidate the physics underlying the electron transfer driven by strong optical fields in plasmonic gaps. Especially, we clarify the interplay between carrier-envelope phase of the driving pulse, plasmonic resonance and quiver motion.

Femtosecond pulses consisting of only a few cycles of the optical carrier wave [1] have enabled breakthrough opportunities for the direct manipulation of electrons in condensed matter based on nonlinear phenomena as well as in free space via linear acceleration [2-18]. The traditional conditions for such control experiments required extreme pulse intensities at low repetition rates, imposing substantial difficulties for the extraction of the dynamics of individual charge carriers. Recently, several works paradigmatically changed the approach to exploit optical phenomena driven by strong fields by employing pulses with minute energy content at high repetition rates, thus allowing for generation and manipulation of photoelectrons in nanoscale systems [4,19,20].

In this context, single-cycle pulses with an energy of only a few picojoules may result in extremely nonlinear optical phenomena within a few-nanometer gap between the tips of an optical antenna [19,21-25]. The strong electrical

33 bias provided by the field contained in the ultrashort optical pulses was harnessed to drive tunneling and ballistic
 34 acceleration of electrons generating a current with PHz bandwidth [19,26]. This non-perturbative process is fully
 35 coherent with the driving radiation and occurs within a half-cycle of the near-IR carrier wavelength [19]. Here, by
 36 performing interferometric autocorrelation measurements with two identical replicas of truly single-cycle driving
 37 pulses, we directly access the attosecond dynamics of the optical field emission and electron transport in plasmonic
 38 gaps. Controllable variation of the carrier-envelope phase (CEP) of the pulses enriches the experimental acquisition
 39 of the interferometric traces by an additional variable that allows for a deep understanding and complete insight
 40 into the relationship between the photo-emitted electrons and the accelerating field. Time-dependent density
 41 functional theory (TDDFT) calculations of the optical field emission and subsequent acceleration of the electrons in
 42 the plasmonic gap accurately reproduce the experimental results. In this way, we elucidate the underlying
 43 microscopic phenomena, including visualization of the evolution of electron currents in time and space as a
 44 function of the CEP of the driving pulses.



45
 46 **Fig. 1(a)** Conceptual sketch of the experiment with two single-cycle light pulses delayed by a time Δt and focused on the
 47 nanocircuit. The relative CEP of the biasing pulses can be fully controlled with a precision of 10 mrad. The image includes
 48 a scanning electron micrograph of the Au optical antenna with electrical leads on a fused-silica substrate and a zoom into
 49 the gap region (inset). The red arrow sets the positive direction of the electric field, and the white arrow gives the
 50 corresponding direction of the electron transfer. (b) Temporal profile of the optical field when set to a cosine phase in
 51 free space (CEP=0), as characterized by 2D spectral shearing interferometry [27]. (c) The pulse-averaged current induced
 52 by the electric field of light. At the pulse repetition rate of 80 MHz the transfer of one electron per pulse corresponds to a
 53 current of 12.8 picoamperes. Results are shown as a function of the free-space amplitude of the electric field of the laser
 54 pulse. The current is modulated sinusoidally with a phase ϕ that is directly related to the far-field CEP of the driving pulse
 55 $\phi = \text{CEP} + \delta$. Since only the relative CEP can be defined experimentally, δ is unknown. The phase of the current variation ϕ
 56 is then defined such that $\phi=0$ corresponds to the maximum current, and this reference is used to assign the values in
 57 panel (c). The dotted line reports the TDDFT result obtained for the phase conditions of the pulse corresponding to the
 58 maximum electron transfer.

59
 60

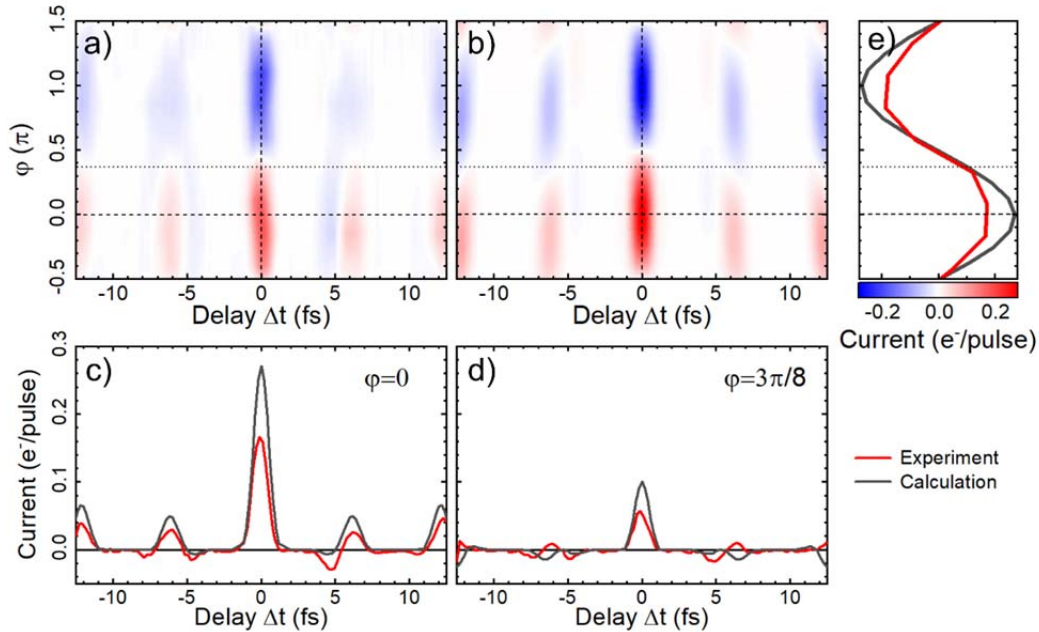
61 Figure 1(a) depicts the conceptual scheme of the experiment. The single-cycle pulses are set at a variable delay Δt
62 by a broadband dispersion-balanced Mach-Zehnder interferometer and then focused tightly onto the nanocircuit
63 containing a single plasmonic bowtie antenna. The Au nanoantenna features a 6 nm open junction and was
64 fabricated via electron beam lithography (inset in Fig. 1(a)). Under a quasi-static electric bias, this structure exhibits
65 a tunneling-like current-voltage (I-V) characteristic that is antisymmetric and highly nonlinear [19]. The bowtie
66 design allows for a sub-wavelength concentration of the electric field of the laser pulse into the gap while at the
67 same time preserving its single-cycle character owing to the strong radiation damping [25].

68
69 A custom-designed Er:fiber laser system [1,28] operates at a repetition rate of 80 MHz and generates 4.2-fs pulses
70 from a tailored supercontinuum spanning from 800 nm to 2200 nm generated in a highly nonlinear germanosilicate
71 fiber. After compression, the optical transients have a full-width-at-half-maximum (FWHM) duration that
72 corresponds to a single cycle of the carrier wavelength at 1250 nm. Such single-cycle pulses are ideal for driving
73 ultrafast transport experiments that exploit a non-perturbative phenomenon such as optical field emission [19].
74 The temporal profile of the pulses is characterized in Fig. 1(b). A passive phase-locking scheme [29] is implemented
75 in a way that allows arbitrary control of the carrier-envelope phase without affecting the temporal duration of the
76 pulse [19]. These optical transients provide a strong and ultrafast bias for direct and coherent driving of electronic
77 transport across the junction. Due to the strong nonlinearity of the optical field emission process, an optically-
78 induced symmetry break occurs in the electric transport which leads to a net current that depends on the carrier-
79 envelope phase of the driving pulse. Consequently, when sweeping the carrier-envelope phase over a range of 2π ,
80 the integral current passes through a maximum, crosses zero and finally completely reverses its direction.

81
82 For the autocorrelation measurements, the current generated at the nanojunction of the circuit is recorded as a
83 function of both the delay between the two pulse replicas and their carrier-envelope phase. These measurements
84 were performed in air and at room temperature over several minutes. They demonstrate excellent reproducibility
85 of the current signal and high stability of the nanostructure, as indicated by the traces depicted in figure 1(c) that
86 report the current measured as a function of the optical field amplitude of the single-cycle pulses. This dataset was
87 acquired at different relative CEP of the driving pulses on a single sample. Note that since the absolute value of CEP
88 cannot be defined experimentally, in figure 1(c) we assign the results according to the phase of the sinusoidal
89 modulation of the current, φ . This reference phase is set to zero, $\varphi = \varphi_0 = 0$, for the situation that shows the
90 maximum positive value of the current. In our experiments, the phase shift δ between the absolute value of the far-
91 field CEP and φ is approximately $\pi/2$, as assessed by the numerical calculations. At perfect temporal overlap
92 between the two pulses (i.e. delay $\Delta t = 0$ fs, equivalent to a single pulse), the average optical power amounts to 1.7
93 mW. This value still corresponds to a minute driving pulse energy of 21 pJ and a free-space peak field of 1 V/nm at
94 the sample position within the confocal spot of the objective (1.5 μm spot size). Owing to the implementation of

95 smaller gaps and a shorter pulse, we achieve a four-fold increase in the current at a factor of four lower driving
 96 energy as compared to our previous results [19], allowing interferometry measurements with an unprecedented
 97 access to a complex dynamics of electron currents within the gap. The experimental data obtained with a single
 98 pulse are reproduced with our TDDFT calculations allowing to retrieve the amplitude of the electric field in the gap,
 99 as well as to identify the absolute value of the CEP that provides the maximum positive current (also see the SI).

100



101

102 **Fig. 2** Colour map of the measured (panel a)) and calculated (panel b)) two-dimensional interferometric autocorrelation
 103 acquired as a function of temporal delay Δt and phase φ of the sinusoidal current modulation. (c) Interferometric
 104 autocorrelation (red line) of two identical single-cycle pulses with CEP set to deliver the maximum peak current using the
 105 current driven at the nanogap as nonlinear signal (dashed line in (a) and (b)). The extreme order of nonlinearity is
 106 underlined by the absence of signal when the maxima of the field do not overlap at the periodicity of the carrier
 107 wavelength. The width of the central peak amounts to approximately 1 fs. The experimental data is compared with the
 108 equivalent trace derived from the calculations (black line). (d) same as (c) but acquired at $\varphi = 3\pi/8$ (dotted line in (a)
 109 and (b)). (e) Vertical cut of the 2D colour map at $\Delta t = 0$, i.e. equivalent to single pulse illuminating the nanogap. The
 110 sinusoidal modulation of the current with the phase φ is shown for experiment (red line) and theory (black line).

111

112 Figure 2(a) presents the full 2D map of the interferometric autocorrelation that depicts the nonlinear ultrafast
 113 current driven by a pulse pair as a function of their relative time-delay Δt , and CEP. The colour code from blue to
 114 red follows the amplitude and direction of the electron transfer. The 2D map of electron transport contains
 115 information that goes well beyond standard interferometric autocorrelation measurements based on optical

116 nonlinear signals where a one-dimensional fringe pattern is acquired as a function of the temporal delay between
117 the pulses. Specifically, it contains one additional degree of freedom on the ordinate: the modulation of the current
118 by varying the CEP encoded in the single-cycle optical fields. Simultaneous access to both the temporal delay and
119 the carrier-envelope phase dependence of electron transport allows unveiling the complex non-perturbative
120 phenomenon of optical field emission in a nanogap and provides unprecedented details to be exploited in
121 combination with theoretical approaches, as presented in this work. In Fig. 2(b) the theoretical 2D autocorrelation
122 map shows an excellent qualitative agreement with the experimental one (Fig. 2(a)). The quantitative comparison
123 between experiment and calculations is presented in Fig. 2(c) and Fig. 2(d) which include a cut of the map at a fixed
124 value of the reference phase φ , and can be conceptually compared to a standard interferometric autocorrelation
125 measurement. The results in figure 2(e) display the dependence of the electron transfer on φ (and thus on the CEP
126 as $\text{CEP} = \varphi + \delta$) at zero time delay, demonstrating full CEP control of the electron currents with a single optical pulse.

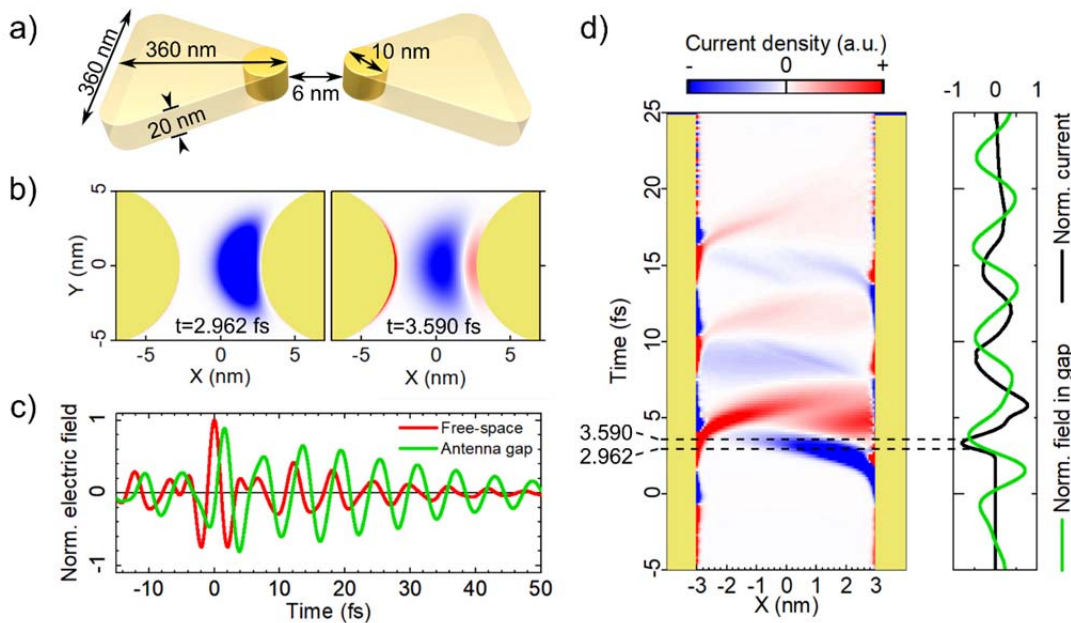
127
128 From this dataset, it becomes clear that the interferometric autocorrelation originates from a highly non-
129 perturbative process operating on a sub-femtosecond time scale. The interference maxima are significantly shorter
130 than an optical half-cycle of the driving field, featuring a FWHM of approximately 1 fs. In addition, the
131 autocorrelation signal completely vanishes between the constructive maxima, and the amplitude of the side peaks
132 is strongly reduced with respect to the situation of perfect overlap. Importantly, these findings clearly demonstrate
133 that the electronic transport in the junction is directly connected with the phase of the driving pulse, and that the
134 current dynamics of electronic wavepackets can be controlled on the timescales shorter than a half-cycle of the
135 optical field.

136
137 To gain microscopic insight into the spatio-temporal electron dynamics induced by the optical field in our
138 nanodevice, we carry out first-principles TDDFT [30] simulations, a very powerful tool in the description of the
139 strong field phenomena at metal surfaces [31-33]. While a full quantum calculation is out of reach for mesoscopic
140 objects like the Au bowties used in the experiments, the main physics can be captured with the reduced system
141 sketched in figure 3(a). Indeed, for the bowtie used in our experiments the height $h=20\text{nm}$ is essentially larger than
142 the size of the gap and the plasmonic field enhancement strongly confines the region of optical field emission and
143 electron transport to the junction, as follows from the snapshots of the calculated electron current density
144 depicted in figure 3(b). We then model the plasmonic gap as two infinite parallel Au cylinders described within the
145 free electron (jellium) model. The cylinder radii R_c and their separation distance d_g are adapted to the shape of the
146 antenna as visualized by the SEM images ($R_c=5\text{nm}$ and $d_g=6\text{nm}$). Since the optical response of the nanowire dimer is
147 different from that of the actual bowtie antenna, special care is needed to correctly capture the optical field
148 emission from the metal surfaces facing the gap in the experimental situation. To this end, in the TDDFT
149 calculations, the incident sub-cycle pulse is set such that the time trace of the self-consistent electric field in the

150 gap of the cylinder dimer is equivalent to the one obtained from classical Maxwell's equations for the actual bowtie
 151 antenna (for further details see SI). The absolute value of the field is calibrated with respect to the experimental
 152 dependence of the current on the pulse energy (see theoretical result in figure 1(c) plotted as grey line with dots).

153
 154 The effect of the plasmonic resonance in the near-field at the gap region of the bowtie nanoantenna may be seen
 155 in Fig. 3(c). The far-field transient (red line) of a pulse with CEP = 0 in free space becomes distorted within the
 156 antenna gap (green line). The field in the junction is enhanced by two orders of magnitude in line with the data
 157 obtained with classical calculations in the literature [11,34]. In addition, a phase shift $CEP_{gap} - CEP \approx 0.35\pi$ occurs
 158 between the effective phase of the pulse in the near-field of the gap, CEP_{gap} , and that of the far-field transient. This
 159 value is obtained from the time dependence of the fields close to $t=0$ within the central part of the pulse. The
 160 plasmon resonance of the nanoantenna results in a few-cycle ringing of the near-field with a characteristic phase
 161 shift of $\pi/2$ at large times following the main peak. We show that, in analogy with experiments on multiphoton
 162 electron emission from flat metal surfaces [35], an excitation of the antenna plasmon in the present case has a
 163 strong effect on the autocorrelation traces.

164



165
 166 **Fig. 3(a)** Conceptual sketch of the antenna geometry employed for the calculations. The cylinders reproducing the
 167 morphology of the antenna apices are used in the TDDFT calculations of the optical field emission while the plasmonic
 168 resonance corresponding to the whole bowtie antenna gap is captured by solving the classical Maxwell's equations. (b)
 169 Snapshots of the electron current density within the gap at two different instants of time indicated with dashed lines in
 170 panel d). The reference time $t=0$ is set at the maximum of the free-space optical field. (c) Electric field profile of the far-
 171 field illumination of a pulse with CEP=0 (red) and corresponding electric field profile calculated in the centre of the gap

172 (green). The fields in the antenna gap are scaled by a factor of 1/100. (d) Left: colour map of the electron current along
173 the dimer axis, calculated as a function of time for far-field illumination with CEP=0. Right: corresponding electric field in
174 the gap (green) and integrated electron current across the gap central plane (black). The metal volume is shaded with
175 yellow rectangles.

176
177
178 The enhanced electric field in the junction region drives the optical field emission and thus the electron flow
179 through the gap, as illustrated in figure 3(d). For an illumination pulse with a CEP=0 in free space, the antenna
180 resonance shapes the temporal profile of the transient to become almost sine-like in the near-field with an
181 effective phase $CEP_{\text{gap}} = 0.35\pi$ (see Fig. 3(c)). This effect, combined with the temporal dynamics of the electrons
182 within the gap, leads to two opposite electronic streams – which are produced by the central cycle of the pulse and
183 which almost completely cancel out each other. The net electron transport through the gap is therefore close to
184 zero in this situation. The entire dynamics is repeated by the following cycles at strongly reduced magnitudes
185 because of the progressive decay of the induced near-field.

186
187 The finite propagation time of the photoemitted electrons through the antenna gap explains an additional offset of
188 the oscillation of the current through the centre of the junction with respect to that of the field in the gap.
189 Noteworthy, for the present geometry, the trajectories followed by the electrons differ from what is typically
190 observed in the case of metal tips. For optical field emission from nanotips or individual plasmonic nanoobjects, the
191 fast spatial decay of the electric near-fields reduces the quiver motion of emitted electrons [2,10,11,31]. However,
192 contrary to the case of a single nanoparticle, the electric field in a metallic gap is rather spatially uniform. This fact
193 renders the dynamics of electron transport to be strongly affected by the quiver motion as illustrated in Fig. 3(d). In
194 detail, similar to Fowler-Nordheim emission in strong dc fields [31], the early electrons are ejected from the right
195 surface by the strong positive optical field during the first half-period of the pulse with maximum at $t \sim 2$ fs. These
196 electrons appear as a current burst propagating from the right to the left within the gap. The initial acceleration
197 within the gap is sketched in the left snapshot of figure 3(b). Since the driving pulse is almost sine-like in the near
198 field, the polarity of the field changes within the second half-cycle of the pulse, when the electrons are still within
199 the gap. As a result, part of the electrons belonging to the initial burst experience a complete reversal of sign in the
200 propagation direction (seen as change of the sign of the electron current density from blue-negative to red-positive
201 going through white-zero) approximately at the centre of the junction. This situation is depicted in the right
202 snapshot of Fig. 3(b) where the red region corresponding to positive current density within the gap appears at
203 positive values of the x-coordinate. The positive current density at the negative values of the x-coordinate
204 corresponds to the electrons ejected from the left surface by the strong optical negative field during the second
205 half-period of the pulse with an extremum value at $t \sim 4$ fs (see also Fig. 3(d)). The quiver motion of the ejected

206 electrons is further illustrated with classical electron trajectories in Fig. S9 of the Supporting Information which
207 provides a classical analogue to the results of TDDFT calculations in Fig. 3(d).

208
209 In the present case, the amplitude of the quiver motion $X_Q = E_g/\omega^2$ (E_g is the maximum value of the field in the
210 gap and ω is the central frequency of the pulse, all values are expressed in atomic units), is such that the electron
211 excursion $2X_Q$ is essentially smaller than the size of the gap, thus enabling coherent motion of the ejected
212 electrons. This aspect has a direct consequence on the CEP conditions for the maximum electron transport to occur
213 since a significant number of the electrons do not cross the junction directly, but experience a quiver motion with
214 several reversals of the direction of propagation before crossing the gap (the examples of the classical electron
215 trajectories can be found in SI). The dynamics of the electron currents is further complicated by the presence of the
216 small fraction of electrons re-scattered from the parent tip and from the opposite tip across the junction.
217 Nevertheless, the optimal CEP provides a drift velocity such that the electrons emitted at the central part of the
218 pulse cross the junction. In fact, we calculate that the maximum electron transfer is reached for CEP = 0.48π of the
219 far field transient resulting in the effective phase CEP_{gap} = 0.84π of the central part of the pulse in the near field of
220 an antenna gap (see figure S8 of the Supporting Information). Therefore, the match between the measured and
221 calculated sinusoidal modulation of the current at delay $\Delta t = 0$ fs in figure 2(e) allows us to unambiguously
222 determine the absolute value of the free-space CEP in the experiment. Along with the possibility to determine the
223 CEP of the experimental transient, the remarkable agreement between the modelled and experimental results also
224 reveals the role of the plasmon mode of the nanoantenna. It follows from our calculations that the secondary
225 maxima in the experimental autocorrelation plot in figure 2(c) emerge owing to the overlap of the strong fields at
226 the central part of the second replica with the resonantly enhanced near-fields at large time delays following the
227 first pulse. In fact, in the ideal case of a flat antenna response, the autocorrelation signal obtained with TDDFT is
228 zero at every time delay except for the central cycle.

229
230 In both measured and calculated data, the CEP-dependence of the secondary maxima is slightly phase-shifted with
231 respect to the main peak. This result stems from: (i) the non-gaussian, asymmetric profile of the driving pulse for
232 which the slowly varying envelope approximation is not valid (i.e. the carrier cannot be considered monochromatic)
233 and thus may be affected by some residual chirp; (ii) the resonance effect of the plasmonic antenna that shapes the
234 field within the gap and defines the quiver motion of electrons emitted at different instants of time. This aspect
235 becomes even clearer in the interferometric autocorrelation plotted in figure 2(d). The experimental data (red
236 lines) and theoretical results (black lines) correspond to the constant phase $\varphi = 3\pi/8$ cut of the autocorrelation
237 maps of figure 2(a) and (b). The signs of the secondary maxima are reversed with respect to the ones of the main
238 peak at $\Delta t = 0$. Altogether, the high nonlinearity of the optical field emission allows for using our device as a
239 sensitive probe of the dynamics of the near fields in plasmonic gaps.

240
241 In conclusion, we have performed interferometric autocorrelation measurements with single-cycle pulses that
242 exploit the electric currents coherently driven at the gap of a single nanodevice. These measurements operate in an
243 extremely nonlinear regime that is achieved even at minute pJ pulse energies. Along with optical field emission, a
244 complex dynamics for the field-driven transport of the electrons emerges in the free space between the metal
245 surfaces that determines the electron currents in the system and offsets the carrier-envelope phase of the driving
246 field that produces maximum electron current. Remarkably, the extreme temporal resolution that we achieve in
247 performing current autocorrelation measurements demonstrates that we can control the transfer of individual
248 electrons between two metallic nanocontacts and access the evolution of plasmonic fields in the nanogap at a
249 subcycle time scale. In such a scenario, the photoemitted electrons experience quiver motion, which responds to
250 the complex temporal structure of the fields induced in the gap, resulting in a shift of the phase at which the
251 maximum current is obtained. Therefore, tracing and dissecting an ultrashort photocurrent in a plasmonic nanogap
252 is found to be crucial for the proper design of integrated plasmonic and optoelectronic devices that operate in the
253 single-electron regime at optical frequencies. In addition, the theoretical developments and fundamental
254 understanding of electronic dynamics driven at the nanoscale by optical fields, as achieved in this work, will allow
255 to target future experiments where electron transport is confined to truly atomic time and length scales.

256

257 **Methods**

258 Methods and any associated references are available in the online version of the paper.

259 ***Source of control transients***

260 The elements of the Er:fiber laser system providing the ultrashort optical control pulses exploited in our experiment are
261 described in detail in Ref. 16. Here, for the first time, single-cycle near-infrared transients that are passively phase locked were
262 generated at a repetition rate as high as 80 MHz by combining super-octave-spanning coherent synthesis with elimination of the
263 carrier-envelope phase slip via difference frequency mixing and re-amplification. The present implementation of the system is
264 even superior to our earlier results in terms of pulse duration [1]. The laser system also offers precise CEP control by placing a
265 pair of fused-silica wedges before the last Er:fiber amplifier and final compression. The minimum duration is achieved by
266 independent compression of soliton and dispersive wave (with a three-prism setup) before coherent combination of the two
267 spectral components produced by a highly nonlinear fiber.

268 For a full temporal reconstruction of the pulse we performed a direct characterization via two-dimensional spectral shearing
269 interferometry. This method allows direct reconstruction of the electric field profile, i.e. the amplitude and the phase of the
270 electromagnetic wave. It is particularly suited for super-octave-spanning spectra. By fine tuning the dispersion via an SF10 prism
271 pair, we obtain an almost flat phase over the entire spectrum. This result corresponds to a pulse duration of 4.2 fs and 1 optical
272 cycle at the central wavelength of 1250 nm. The complete characterization is included in the Supporting Information.

273

274 **Antenna fabrication and characterization**

275 The nanostructured electronic circuit equipped with a plasmonic antenna was fabricated by electron beam lithography. A fused
 276 silica window was spincoated with a 60 nm layer of PMMA (950k) resist. Heating the substrate above 100°C before deposition
 277 evaporates residual water on the surface. An 8 nm-thick thermally evaporated layer of aluminum provided the necessary
 278 electric conduction to avoid distortion due to charging effects during exposure. The structures were written with an area dose of
 279 400 pC/cm² at 10 kV. Subsequently, the aluminum layer was removed in a bath of sodium hydroxide followed by a rinse in
 280 deionized water. Development of the resist was carried out in a mixture of methyl isobutyl ketone (MIBK), methyl ethyl ketone
 281 (MEK) and isopropanol (IPA) in a volume ratio of 100:6:300. The gold nanostructures were patterned in a subsequent
 282 evaporation process in which 18 nm of gold were evaporated on top of a 2 nm chromium adhesion layer followed by a lift-off
 283 process in a bath of acetone. The electronic interface between the nanostructures and the detection electronics was provided
 284 by a custom-made circuit board into which the fused silica substrates were integrated and connected by wire bonding.

285

286 **TD-DFT**

287 The dynamics of the electron density induced by a laser pulse has been obtained by solving the time-dependent Kohn-Sham (KS)
 288 equations [30].

289
$$i\partial_t\psi_k(\vec{r}, t) = \{T + V_{Au} + V_{xc}(n) + V_H(n) + V^{ext}(t)\} \psi_k(\vec{r}, t). \quad (1)$$

290 This equation describes the evolution of the quasiparticle Kohn-Sham (KS) orbitals ψ_k under the action of an external potential
 291 V^{ext} . The incident laser pulse is treated within the dipole approximation. In the Coulomb gauge the external potential is given
 292 by $V^{ext} = E^{ext}(t)x$, where $E^{ext}(t)$ describes the external field, and the dimer x -axis is defined in Fig. 3a. In Eq. (1) T is the
 293 kinetic energy operator, V_{Au} describes the electron interaction with atomic cores, $V_{xc}(n)$ is the exchange-correlation potential
 294 treated within the adiabatic local density approximation [30] with exchange-correlation kernel of Gunnarson and Lundquist [36],
 295 and $V_H(n)$ is the Hartree potential. The time-dependent electronic density of the system is given by $n(\vec{r}, t) = \sum_{k=occ} |\psi_k(\vec{r}, t)|^2$
 296 where the summation runs over the occupied KS orbitals. The initial conditions $\psi_k^0(\vec{r})$ are given by the KS orbitals of the ground
 297 state system, obtained from the ground-state density functional theory (DFT) calculation,

298
$$\underbrace{\{T + V_{Au} + V_{xc}(n_0) + V_H(n_0)\}}_{H_0} \psi_k^0(\vec{r}) = E_k \psi_k^0(\vec{r}), \quad (2)$$

299 where the Hamiltonian H_0 depends on the ground-state density via the exchange-correlation and Hartree potentials. Consistent
 300 with TDDFT, the exchange-correlation kernel of Gunnarson and Lundquist is used for $V_{xc}(n_0)$, where $n_0(\vec{r}) = \sum_{k=occ} |\psi_k^0(\vec{r}, t)|^2$.

301

302 Considering the dimer of two infinite cylindrical nanowires with $d_g = 6$ nm as a reduced model mimicking the bowtie antenna
 303 gap brings the system within reach of quantum calculations if the free electron (jellium) description of the metal [37] is used.
 304 Within the jellium model (JM) the ionic cores at the gold lattice sites are replaced by the uniform positive background charge of
 305 density $n_+ = \left[\frac{4\pi}{3} r_s^3\right]^{-1}$. We use $r_s=3$ a₀ characteristic for the valence electron density of gold (a₀=0.053 nm stands for the Bohr
 306 radius). At the price of losing atomistic details, this approach allows us to follow the dynamics of the valence electrons of the
 307 metal involved in the screening, optical field emission, and electron transport [9,31-33,38]. Note also that the JM has been

308 successfully employed in the context of plasmonics allowing theoretical prediction of quantum effects later confirmed
 309 experimentally [24].

310
 311 The reduced model cylindrical nanowire dimer reproduces well the optical field electron emission and electron transport in the
 312 gap of the realistic bowtie antenna. However, the exact description of the electric field induced in the gap region, including the
 313 macroscopic effect of the actual triangular dimer, is of paramount importance for capturing the details of the electron emission
 314 and transport. To this end we solve the classical Maxwell's equations, and we calculate the field in the gap $E_g(t)$ for the actual
 315 silica-supported bowtie nanoantenna subjected to the experimental incident pulse. (As a reference we use the field $E_g(t)$ in the
 316 center of the junction). In the TDDFT calculations, $E^{ext}(t)$ is then set in such a way that the self-consistent field in the gap
 317 equals to $E_g(t)$. The absolute value of the electric field strength used in the TDDFT calculations has been set such that the
 318 experimental data obtained with $\Delta t = 0$ and the CEP corresponding to the maximum electron transfer are reproduced as shown
 319 in figure 1. For a transfer of 0.2 electrons per pulse, we found that the field in the gap is of the order of 10 V/nm and used this
 320 value for all the TDDFT calculations. This fact implies an 11-fold enhancement of the free-space electric field which is
 321 significantly lower than the theoretical estimate based on the solution of the classical Maxwell equations. However, it has to be
 322 considered as an effective value accounting for the experimental uncertainties, as well as for the model geometry used in the
 323 TDDFT study, and possible nonlinear effects leading to a strong reduction of the field enhancement as compared to the
 324 predictions of the classical linear theory [39].

325
 326 Provided the time-dependent solutions of the KS equations $\psi_k(\vec{r}, t)$, one can obtain the time-dependent probability current
 327 density

$$328 \quad \vec{j}(\vec{r}, t) = -i \sum_{k=occ} \frac{1}{2} \{ \psi_k^*(\vec{r}, t) \vec{\nabla} \psi_k(\vec{r}, t) - \psi_k(\vec{r}, t) \vec{\nabla} \psi_k^*(\vec{r}, t) \}, \quad (3)$$

329 and the total electron current per unit height through the centre of the gap (\hat{e}_x is the unit-length vector along x-axis)

$$330 \quad I(t) = \int \hat{e}_x \vec{j}(\vec{r}, t)|_{x=0} dy. \quad (4)$$

331 The theoretical prediction for the number of electrons transferred across the gap of the bowtie nanoantenna is then given by
 332 $N = h \int_{t_0}^T I(t) dt$, where $h=20$ nm is the height of the nanoantenna. The final propagation time is taken large enough so that the
 333 electric field becomes small and the electron transfer stops.

334
 335 The TDDFT results presented in figure 2 could be reproduced with the use of a classical simple man's model [31] (see SI)
 336 assuming a flat gap geometry, i.e. a simpler and tackable geometry than that used in our TDDFT calculations. Thus, the
 337 calculated two-dimensional interferometric autocorrelation stems from robust underlying physical phenomena such as optical
 338 field emission from the metal surfaces and the subsequent electron motion in the time varying field. Since the time evolution of
 339 the fields in the junction used in the theoretical description takes into account plasmonic effects, we conjecture that the TDDFT
 340 results presented in this work are qualitatively robust with respect to small variations of the system geometry, and with respect
 341 to the JM description of gold.

342

343

344

345 **Data Availability:**

346 The data that support the findings of this study are available from the corresponding author upon reasonable request.

347

348 **Code Availability:**

349 The code and algorithms that support the findings of this study are available from the corresponding author upon reasonable
350 request.

351

352 **References**

353 1. Krauss, G. et al. Synthesis of a single cycle of light with compact erbium-doped fibre technology. *Nat. Photonics* **4**, 33-36
354 (2010).

355 2. Herink, G., Solli, D., Gulde, M. & Ropers, C. Field-driven photoemission from nanostructures quenches the quiver motion.
356 *Nature* **483**, 190-193 (2012).

357 3. Dombi, P., Krausz, F. & Farkas, G. Ultrafast dynamics and carrier-envelope phase sensitivity of multiphoton photoemission
358 from metal surfaces. *J. Mod. Opt.* **53**, 163-172 (2006).

359 4. Krüger, M., Schenk, M. & Hommelhoff, P. Attosecond control of electrons emitted from a nanoscale metal tip. *Nature* **475**, 78-
360 81 (2011).

361 5. Schiffrin, A. et al. Optical-field-induced current in dielectrics. *Nature* **493**, 70-74 (2012).

362 6. Piglosiewicz, B. et al. Carrier-envelope phase effects on the strong-field photoemission of electrons from metallic
363 nanostructures. *Nat. Photonics* **8**, 37-42 (2013).

364 7. Paasch-Colberg, T. et al. Solid-state light-phase detector. *Nat. Photonics* **8**, 214-218 (2014).

365 8. Cocker, T. L. et al. An ultrafast terahertz scanning tunneling microscope. *Nat. Photonics* **7**, 620-623 (2013).

366 9. Gao, C.-Z. et al. Strong-field effects in the photoemission spectrum of the C60 fullerene. *Phys. Rev. A* **93**, 022506 (2016).

367 10. Echtenkamp, K. E. et al. Strong-field photoemission in nanotip near-fields: from quiver to sub-cycle electron dynamics. *Appl.*
368 *Phys. B* **122**, 80 (2016).

369 11. Dombi, P. et al. Ultrafast Strong-Field Photoemission from Plasmonic Nanoparticles. *Nano Lett.* **13**, 674-678 (2013).

370 12. Cocker, T. L., Peller, D., Yu, P., Repp, J. & Huber, R. Tracking the ultrafast motion of a single molecule by femtosecond orbital
371 imaging. *Nature* **539**, 263-267 (2016).

372 13. Ahn, B. et al. Attosecond-controlled photoemission from metal nanowire tips in the few-electron regime. *APL Photonics* **2**,
373 036104 (2017).

- 374 14. Vogelsang, J., Hergert, G., Wang, D., Groß, P. & Lienau, C. Observing charge separation in nanoantennas via ultrafast point-
375 projection electron microscopy. *Light-Sci. Appl.* **7**, 4–11 (2018).
- 376 15. Jelic, V. et al. Ultrafast terahertz control of extreme tunnel currents through single atoms on a silicon surface. *Nat. Phys.* **13**,
377 591-598 (2017).
- 378 16. Yoshioka, K. et al. Tailoring Single-Cycle Near Field in a Tunnel Junction with Carrier-Envelope Phase-Controlled Terahertz
379 Electric Fields. *Nano Lett.* **18**, 5198–5204 (2018).
- 380 17. Yoshioka, K., Katayama, I., Minami, Y., Kitajima, M. & Yoshida, S. (2016). Real-space coherent manipulation of electrons in a
381 single tunnel junction by single-cycle terahertz electric fields. *Nat. Photonics* **10**, 762–765 (2016).
- 382 18. Rácz, P. et al. Measurement of Nanoplasmonic Field Enhancement with Ultrafast Photoemission. *Nano Lett.* **17**, 1181–1186
383 (2017).
- 384 19. Rybka, T. et al. Sub-cycle optical phase control of nanotunnelling in the single-electron regime. *Nat. Photonics* **10**, 667–670
385 (2016).
- 386 20. Putnam, W. P., Hobbs, R. G., Keathley, P. D., Berggren, K. K. & Kärtner, F. X. Optical-field-controlled photoemission from
387 plasmonic nanoparticles. *Nat. Phys.* **13**, 335-339 (2017).
- 388 21. Savage, K. et al. Revealing the quantum regime in tunnelling plasmonics. *Nature* **491**, 574-577 (2012).
- 389 22. Esteban, R. et al., A classical treatment of optical tunneling in plasmonic gaps: extending the quantum corrected model to
390 practical situations. *Faraday Discuss.* **178**, 151-183 (2015).
- 391 23. Wan, Y., Wubs, M. & Mortensen, N. A., Projected Dipole Model for Quantum Plasmonics. *Phys. Rev. Lett.* **115**, 137403
392 (2015).
- 393 24. Zhu, W. et al. Quantum mechanical effects in plasmonic structures with subnanometre gaps. *Nat. Commun.* **7**, 11495 (2016).
- 394 25. Hanke, T. et al. Tailoring spatiotemporal light confinement in single plasmonic nanoantennas. *Nano Lett.* **12**, 992–996 (2012).
- 395 26. Aguirregabiria, G. et al. Dynamics of electron-emission currents in plasmonic gaps induced by strong fields. *Faraday Discuss.*
396 **214**, 147-157 (2019).
- 397 27. Birge, J. R., Ell, R. & Kärtner, F. X. Two-dimensional spectral shearing interferometry for few-cycle pulse characterization.
398 *Opt. Lett.* **31**, 2063-2065 (2006).
- 399 28. Brida, D., Krauss, G., Sell, A. & Leitenstorfer, A. Ultrabroadband Er: fiber lasers. *Laser Photon. Rev.* **8**, 409-428 (2014).
- 400 29. Krauss, G. et al. All-passive phase locking of a compact Er: fiber laser system. *Opt. Lett.* **36**, 540-542 (2011).
- 401 30. Marques, M. A. L. & Gross, E. K. U. Time-dependent density functional theory. *Annu. Rev. Phys. Chem.* **55**, 427-455 (2004).
- 402 31. Krüger, M., Lemell, C., Wachter, G., Burgdörfer, J. & Hommelhoff, P. Attosecond physics phenomena at nanometric tips. *J.*
403 *Phys. B* **51**, 172001 (2018).
- 404 32. Lemell, C., Tong, X., Krausz, F. & Burgdörfer, J. Electron Emission from Metal Surfaces by Ultrashort Pulses: Determination
405 of the Carrier-Envelope Phase. *Phys. Rev. Lett.* **90**, 076403 (2003).

- 406 33. Wachter, G., Lemell, Ch., Burgdörfer, J., Schenk, M., Krüger, M., Hommelhoff, P. Electron rescattering at metal nanotips
407 induced by ultrashort laser pulses. *Phys. Rev. B* **86**, 035402 (2012).
- 408 34. Schuck, P. J., Fromm, D. P., Sundaramurthy, A., Kino, G. S., & Moerner, W. E. Improving the mismatch between light and
409 nanoscale Objects with gold bowtie nanoantennas. *Phys. Rev. Lett.* **94**, 017402 (2005).
- 410 35. Dombi, P., Irvine, S.E., Rácz, P., Lenner, M., Kroó, N., Farkas, G., Mitrofanov, A., Baltuška, A., Fuji, T., F. Krausz, F., & Elezabi,
411 A. Y. *Opt. Expr.* **23**, 24206-24212 (2010).
- 412 36. Gunnarsson, O. & Lundqvist, B. I. Exchange and correlation in atoms, molecules, and solids by the spin-density-functional
413 formalism. *Phys. Rev. B* **13**, 4274-4298 (1976).
- 414 37. Lang, N.D. & Kohn W. Theory of metal surfaces: work function. *Phys. Rev. B* **3**, 1215-1223 (1971).
- 415 38. Nguyen, H.S., Bandrauk, A. D. & Ullrich, C. A. Asymmetry of above-threshold ionization of metal clusters in two-color laser
416 fields: a time-dependent density-functional study. *Phys. Rev. A* **69**, 063415 (2004).
- 417 39. Zuloaga, J., Prodan, E. & Nordlander, P. Quantum plasmonics: Optical properties and tunability of metallic nanorods. *ACS*
418 *Nano* **4**, 5269–5276 (2010).

419

420

421

422

423 **Acknowledgements**

424 DB and AL acknowledge support of the Deutsche Forschungsgemeinschaft through the Emmy Noether programme (BR 5030/1-
425 1) and the collaborative research center SFB 767. DB acknowledges the support by the European Research Council through grant
426 number 819871 (UpTEMPO). GA acknowledges project PI2017-30 of the Departamento de Educación, Política Lingüística y
427 Cultura of the Basque Government, and GA and JA acknowledge funding from project FIS2016-80174-P of the Spanish Ministry
428 of Science, Innovation and Universities MICINN, as well as grant IT1164-19 for consolidated university groups of the Basque
429 Government

430

431 **Author Contributions**

432 JA, AGB, AL and DB conceived the project. AL and DB supervised the experimental activity. ML, FR and TR fabricated the
433 nanostructures, developed the setup and performed the measurements. JA and AGB coordinated the theoretical modeling. GA,
434 D-CM and AGB developed the theory simulations. All authors contributed to the discussion of the data and to the manuscript.

435

436 **Additional information**

437 Correspondence and requests for materials should be addressed to Daniele Brida: daniele.brida@uni.lu

438

439 **Competing financial interests**

440 The authors declare no competing financial interests.

441

442